

**Transient Response of a PEM Fuel Cell  
Representing Variable Load for a  
Moving Vehicle on Urban Roads**

Hamid Naseri-Neshat  
J. W. Van Zee, S. Shimpalee,  
and Woo-kum Lee



**School of Engineering Technology and Sciences**

**University  
Transportation  
Center**

Report Number  
SCSUTC - 444095-01

## **Abstract**

Three-dimensional numerical simulation of transient response of a Polymer Electrolyte Membrane (PEM) fuel cell subjected to a variable load is developed. The model parameters are typical of experimental cell for a 10-cm<sup>2</sup> reactive area with serpentine flow path. Integrated results agree with experiment from previous data. The predictions include transient responses of the cell in terms of local distributions of the current density, water activity, gases mole fraction, velocity, and pressure. The predictions further show that when a step change in time is used to model an abrupt change in the cell voltage, the numerical results show an overshoot for the average transient current density. However, an incremental change of the cell voltage (corresponding to experimental voltage variation due to system response) reduces the peak of current overshoot, and eliminates this overshoot completely if the cell voltage is changed gradually. Therefore, this overshoot is a function of rate of cell voltage change and residence time of the anode and cathode gas flow rates. The extent of local hydration of the membrane is also predicted for the transient conditions.

## Introduction

The issues of acid rain, human health problems related to air-pollution, as well as possible unwelcome changes in the earth's climate, are receiving increasing attention. These problems are in part associated with petroleum-powered vehicles. Automakers are investigating ways for significant reduction of emissions. Alternatives to the internal-combustion engine are being proposed because of the concerns about the health hazards posed by nitrogen oxides in vehicle exhausts and concerns about emissions of the greenhouse gas carbon dioxide. Advanced rechargeable batteries probably will not play a role due to limitations on the speed of charging and the range between charges. DOE's current focus includes the use of a polymer-electrolyte fuel cell (PEMFC) for transportation applications. This is because the PEMFC has a low-temperature operation and ease of construction, and because of its capability to provide a driving range and refuel time comparable to the conventional automobile. Proton Exchange Membrane (PEM) fuel cells producing power for electric drive motors with significantly reduced pollution have been shown to be capable of providing the right power to weight and size ratios for use in automotive applications. Design of fuel cells for Urban Driving applications needs to incorporate transient variation of the amplitude and the frequency of the load changes to integrate the stop and start nature of the driving scenario.

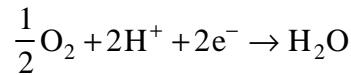
Full three-dimensional solution to the time dependent Navier-Stokes equations for the flow channel and diffusion layers, is developed to investigate the transient behavior of the fuel cell and its performance that can be changed to meet the requirements of the amplitude and the frequency of the load changes. The FLUENT commercial computational fluid dynamics (CFD) solver is used and modified subroutines are added to account for the electrochemical reactions of hydrogen and oxygen by introducing source terms into the transport equations. The complete

three-dimensional Navier-Stokes equations are solved with a control volume based discretization of the computational domain to obtain the velocity and pressure distribution in the flow channels and the gas diffusion layer for every time steps.

The general concept of fuel cell operation is characterized as gas-mixture transport and transformation of species by electrochemical reactions. The hydrogen from anode flow channel is transported through the diffusion layer toward the Membrane Electrode Assembly (MEA) surface. Hydrogen molecules are dissociated to protons and electrons in the catalyst as:



The water that impregnates the MEA hydrates the protons. Electro-osmosis and diffusion transport the water in the MEA. The air mixture in cathode channel is transported through the diffusion layer toward the MEA where oxygen reacts with protons as:



The hydrogen supplies the electrons to one electrode while the oxygen receives them from the other electrode. This flow of electrons produces electricity to power the electric motor of an automobile or other electrical devices. The by-product of this reaction is water, which is the only waste product of PEM fuel cell system.

In preceding studies, models have only focused on the steady behavior of the fuel cell. Some models considered only one-dimensional simulations<sup>1-3</sup>, several models concentrated on two-dimensional flow with transport of the reactants and products in the flow channels and across the membranes<sup>4-11</sup>, and recent models put emphasis on the three-dimensional simulations<sup>12-21</sup>. Merely a single paper published by Um et al.<sup>22</sup> provided a solo figure relating to the preliminary results of their straight channel model. These works have been reviewed by Shimpalee et al.<sup>23</sup>.

In this study, the three-dimensional model of Shimpalee et al.<sup>14</sup> is extended by including time dependent analysis. This is a transient, three-dimensional, isothermal, single phase, and multi-species investigation of a single PEM fuel cell with twenty channels serpentine passes. This work is the first full scale three-dimensional single PEM fuel cell study which integrates a time dependent assessment. Different rates of voltage change are chosen to study their effects on the PEM fuel cell performance at each time step. Moreover, the details of local current density, water activity, and reacting gas concentrations are investigated.

### Model development

This numerical simulation is based on a transient, isothermal, and three-dimensional mass transfer model of a full-cell PEM fuel cell. The actual flow path consists of a serpentine gas channel that has 20 passes as shown in Fig. 1.

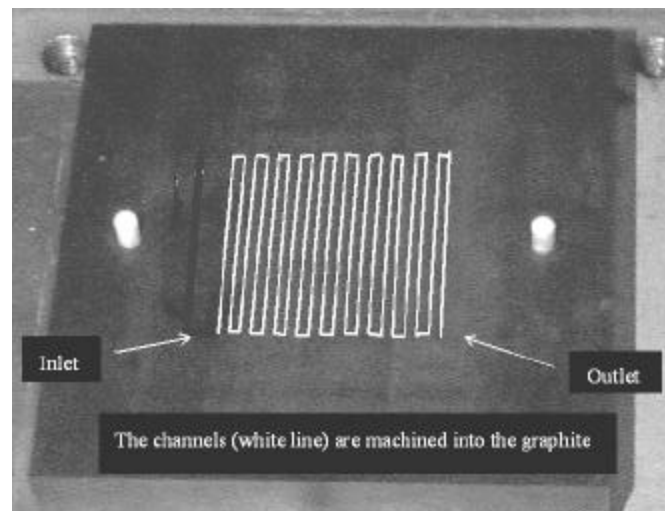


Fig. 1. Actual flow-field plate with 20 serpentine gas flow channels.

Figure 2 shows the modeled channel geometry and the corresponding coordinate system. A thin membrane-electrode-assembly (MEA) is sandwiched between anode and cathode diffusion layers. Anode and cathode side flow channels are symmetric and properly aligned on top of each other<sup>14</sup>.

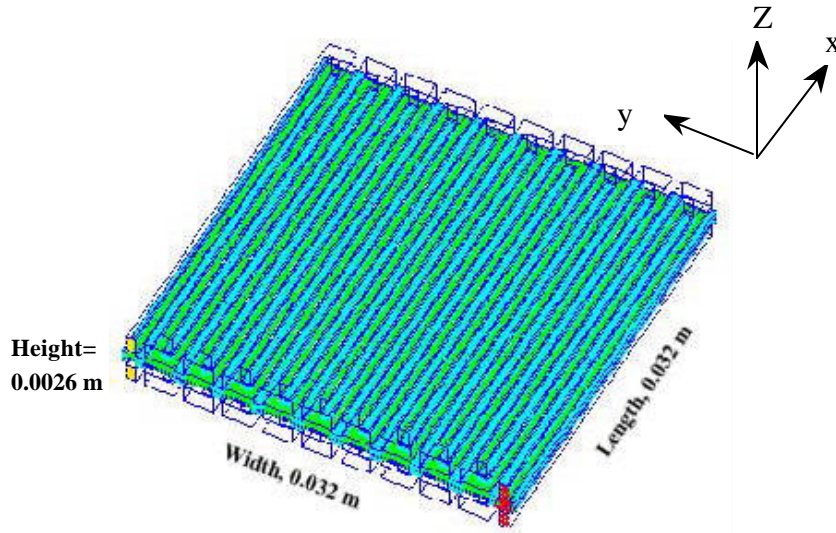


Figure 2. Modeled geometry with actual flow field dimensions.

Figure 3 shows more details of the computational flow domain, which consists of the anode flow channel, anode diffusion layer, MEA, cathode diffusion layer, and cathode flow channel.

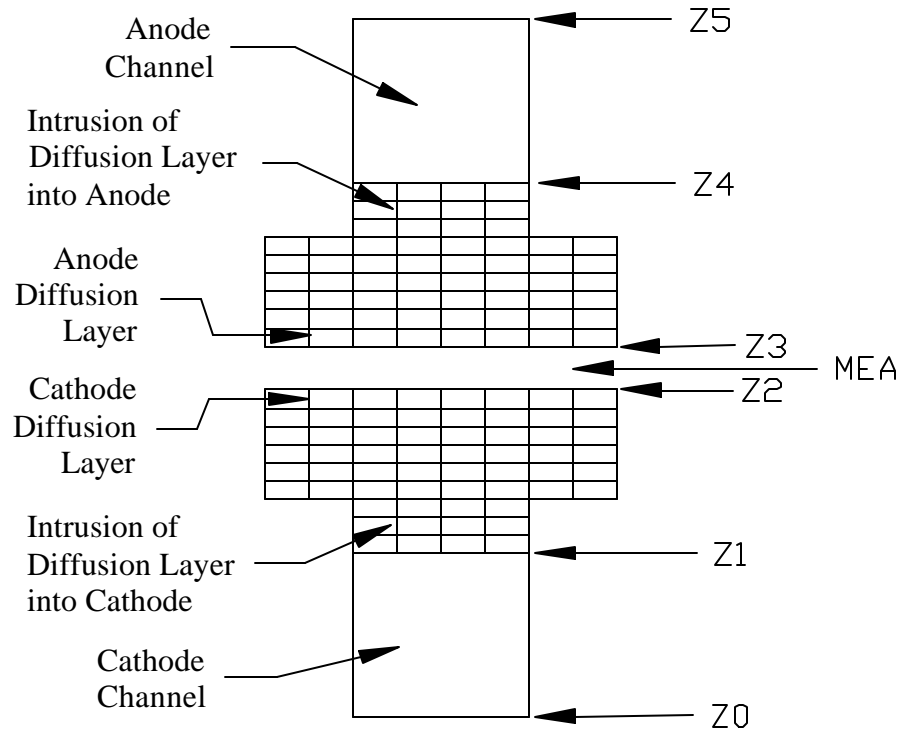


Fig. 3. The detail of computational domain and grid arrangement used in this model<sup>14</sup>.

Fig. 3 further shows different z-locations that are used in defining source terms (see Table 1). The model also takes account of the intrusion of diffusion layers into the gas channels due to the clamping force.

The activities in the membrane are simulated through source terms in the control volumes in contact with the membrane. Species considered are hydrogen, oxygen, nitrogen, and water vapor. The fuel cell operation is characterized as gas transport and transformation of one species to the other. The hydrogen from the anode flow channel is transported through the diffusion layer toward the membrane. Hydrogen molecules are dissociated to protons and electrons in the catalyst and the water that impregnates the MEA hydrates the protons and it is transported by both electro-osmosis and diffusion. The air mixture in the cathode channel is transported through the diffusion layer toward the membrane where oxygen reacts with protons. The water activity in the membrane is simulated by surface based source terms in the control volumes in contact with the membrane.

### Model equations

The time dependent conservation of mass equations (Table 1, Equation 1) in the three-dimensional flow domain is modified to include the electrochemical reactions of a fuel cell by using the respective source terms,  $S_m$ , specified through Equations 7 and 9-12 of Table 1. Note that the source terms are zero in most of the computational domain. These terms corresponds to the consumption of hydrogen in the anode, and the consumption of oxygen and production of water in the cathode. The flux of water is also included as a source term at the anode and cathode (i.e., Equations 10 and 12) by accounting for the diffusion, water content in the membrane, and electro-osmotic drag coefficient as defined by Equations 15, 16, and 17 of Table 2.

The momentum transport equation has a source term within the porous media representing the flow through diffusion layers based on Darcy's law<sup>24</sup>. The addition of this source term effectively converts the momentum equation in the x-direction to  $\frac{\partial P}{\partial x} = -\frac{\mathbf{m}}{\mathbf{b}_x}u$  within the diffusion layer, because  $\beta_x$  is very small and thus the other terms become negligible. A pressure drop is created in the porous layer that is proportional to the mixture velocity in the cell. It can be observed that this source term removes the need for a change in the flow variable as shown in the model of Ref. 9. The permeability,  $\beta_\xi$ , is assumed to be isotropic and it was calculated to be  $3.3 \times 10^{-15} \text{ m}^2$ .

The species transport equations (Equations 3-6 of Table 1) are solved for the mass flow rates of the hydrogen, water, and oxygen species based on the mixture component velocities,  $u$ ,  $v$ , and  $w$ , and the diffusion mass fluxes  $J_{\xi,l}$  for every time step. The species binary diffusion coefficients are calculated as shown by Equation 14 in Table 2. There is one inert component on each side and the concentration of each was determined from a summation of the mass fractions of the other species. Fuller and Newman<sup>4</sup> integrate the flux expression for the diffusion of water through the membrane whereas Refs. 5, 7, and 8 assume a linear gradient as shown by Equation 15. In this study, the diffusion coefficient of each species in the diffusion layer was reduced arbitrarily by 50 percent to account for the effect of porosity and pore-tortuosity. The flux of water through the membrane is critical to the predictions and here we have used the same equation for water content in the membrane as given in Springer et al.<sup>1</sup>. Equation 17 gives relationship between the electro-osmotic drag coefficient and water content in the membrane. This equation is arrived at by curve-fitting the values of water content in the membrane and electro-osmotic drag coefficient as presented in Springer et al.<sup>1</sup>. The diffusion coefficient given in Equation 18 in Table 2 is taken from Nguyen and White<sup>5</sup>.

The expressions for water concentration at the anode and cathode sides,  $C_{w,a}$  and  $C_{w,c}$ , are calculated according to Equation 19, and the activity of water is also defined in Table 2. Moreover, the effects of local hydrogen and oxygen over-potentials are accounted for as shown in Equation 23. These parameters along with the permeability are arrived at through experimental results and attempting to closely match the experimental and numerical VI curves presented in Figure 4. Note that the overall performance (V-I data) for calibration of the input numerical parameters such as over potentials, permeability, etc. using available experimental data, is shown in Table 4. It is important to note that the source terms in Table 1 correspond to the control volume and not the boundary conditions at the anode or cathode interfaces. For the correct determination of the concentrations and activities at the membrane-diffusion layer interface, the mole fraction for each species used in these equations are extrapolated to the membrane surface. A linear extrapolation with the grid of Fig. 2 resulted in a grid independent solution.

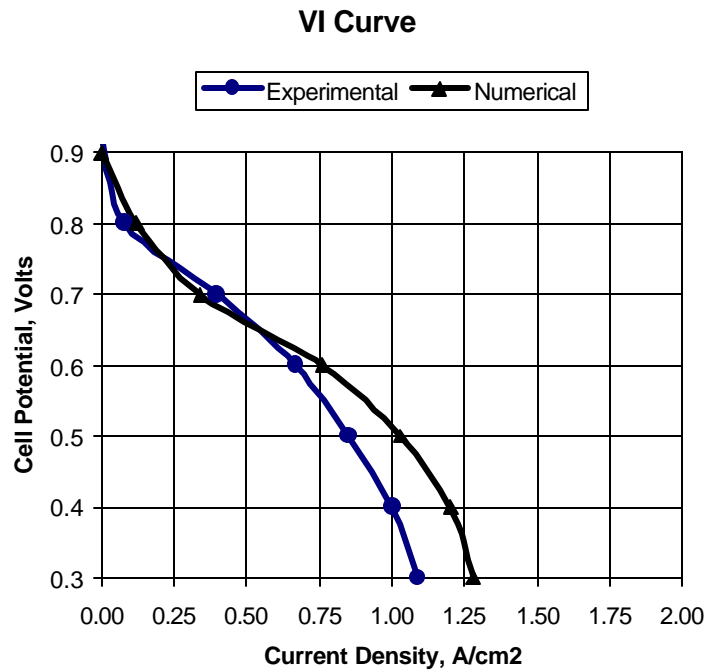


Figure 4. Experimental and numerical VI-curves.

### Numerical procedure

A control volume technique based on FLUENT (version 4.52) commercial flow solver was used to solve the coupled time dependent governing equations. Several subroutines were added to calculate and account for the source terms, permeability, electrochemical reactions, and flux of protons and water across the membrane.

Figures. 2 and 3 show the geometry of fuel cell arrangement modeled in this work, which consists of two flow channels separated by diffusion layers and MEA. There are twenty serpentine passes in the flow path, so that the flow is approximately sixty centimeters long in the axial direction with 0.1 (height) x 0.08 (width) cm<sup>2</sup> cross-section flow area. Each diffusion layer has dimension of 0.025 (height) x 3.20 (width) x 3.20 (length) cm<sup>3</sup>. A total of 34x200x28 cells (elements) were used to model the fuel cell. A separate grid independence test is performed by increasing and decreasing the number of the grid cells on a straight channel. The number of grid cell is decreased and increased by 50 percent of the base case, and predicted results are compared with the base result. The results are less than 2 percent different from each other. Therefore, the numerical grid density that is used for this work is grid independent. The transport of water and proton is simulated by source terms in control volumes in contact with the membrane. The operating pressure is one atmosphere and cell temperature is constant at 70°C. The membrane thickness used in this simulation is 50 microns. Changing of the cell voltage from 0.7 volts at steady state to 0.5 volts, in a single step, and also different incremental alterations, simulate transient variable load for a moving vehicle under stop and go driving condition.

The solution procedure used in this commercial flow solver is based on a SIMPLE algorithm<sup>25</sup>. For every time step, three momentum equations corresponding to three coordinates are solved, followed by a pressure correction equation that does the mass balance. Species

transport equations are solved after the bulk flow calculation. The mixture properties at each control volume are calculated based on the local species content. The anode side gas mixture contains hydrogen and water vapor. On the other hand, the cathode side gas mixture contains oxygen, water vapor, and nitrogen. Therefore, the density and viscosity of the two flow channels are different and vary from one location to the other. Note that, the solution procedures for time-dependent flows used in this model is fully implicit scheme<sup>25</sup>. In this work, the effects of the rate of change in cell voltage on cell performance are studied. Figure 5 shows three different rates of cell voltage changes, which are step change (condition #1), and two types of incremental changes (conditions #2 and 3). The flow rates for this study corresponds to 1.2 anode stoic and 2.0 cathode stoic at cell voltage of 0.5V and details of the operating conditions are shown in Table 3. The initial condition is considered when PEM fuel cell is in a steady state at operating conditions corresponding to stoic for 0.5 volts but the cell voltage is at 0.7V.

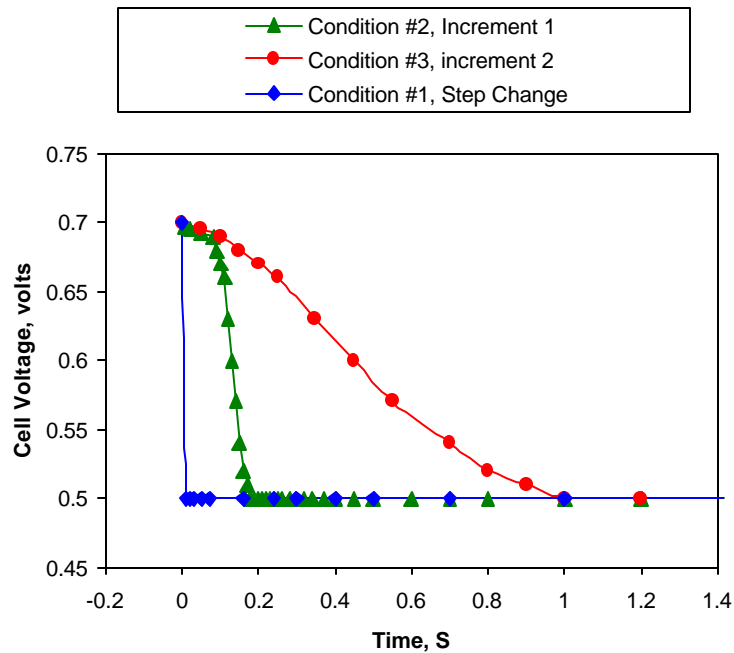


Fig. 5. The difference of cell voltage changes with time used in this study.

## Results and discussion

Fig. 4 shows the transient average current density response when the changes in cell voltages are step and incremental as shown in Fig. 5. The cell voltage increment change in this figure corresponds to condition #2 of Fig. 5.

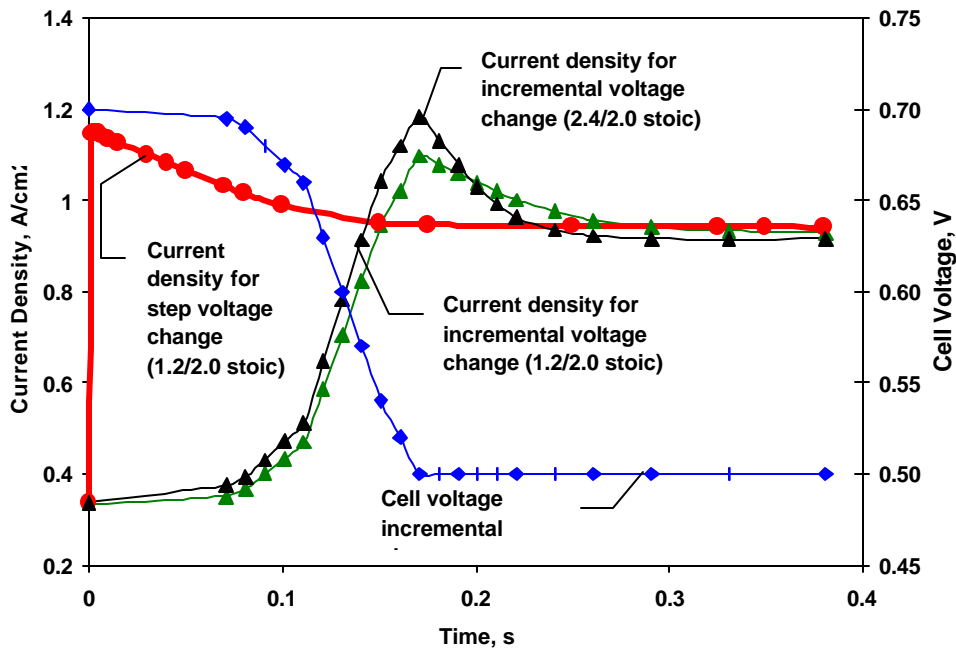


Fig. 6. Transient response of average current density for cell voltage step change cell and voltage incremental change from 0.7V to 0.5V.

Moreover, there are two different anode flow rates used for cell voltage change of condition #2, which are for stoics of 1.2 and 2.4 at 0.5V. In this figure when the cell voltage is changed in one time step from 0.7 V to 0.5 V, the average current density rapidly increases from 0.35 A/cm<sup>2</sup> to 1.15 A/cm<sup>2</sup>. Then the current density decreases with time and reaches steady state condition at  $t=0.17s$  with the average current density of 0.95 A/cm<sup>2</sup>. When the rate of cell voltage change is reduced in several time steps from 0.7 V to 0.5 V as shown in condition #2

with anode stoic of 1.2, the current density begins to increase with time and reaches the maximum average current density of  $1.10 \text{ A/cm}^2$  at  $t=0.18 \text{ s}$ . Again, the current density decreases until  $t=0.35 \text{ s}$  when it reaches the steady state value of  $0.95 \text{ A/cm}^2$ . When the anode stoic is increased to 2.4, the maximum current reaches  $1.21 \text{ A/cm}^2$  at  $t=0.18 \text{ s}$ . Figure 6 shows that the average current density overshoots its steady state value corresponding to that of the cell voltage of 0.5 volts. Moreover, the peak of current overshoot depends on the rate of change of the cell voltage. This figure further reveals that the amount of gas flow rate is one of the parameters, which controls the magnitude of the current overshoot. Higher gas flow rates result in greater current overshoot, but it takes longer to reach steady state as compared to lower gas flow rates.

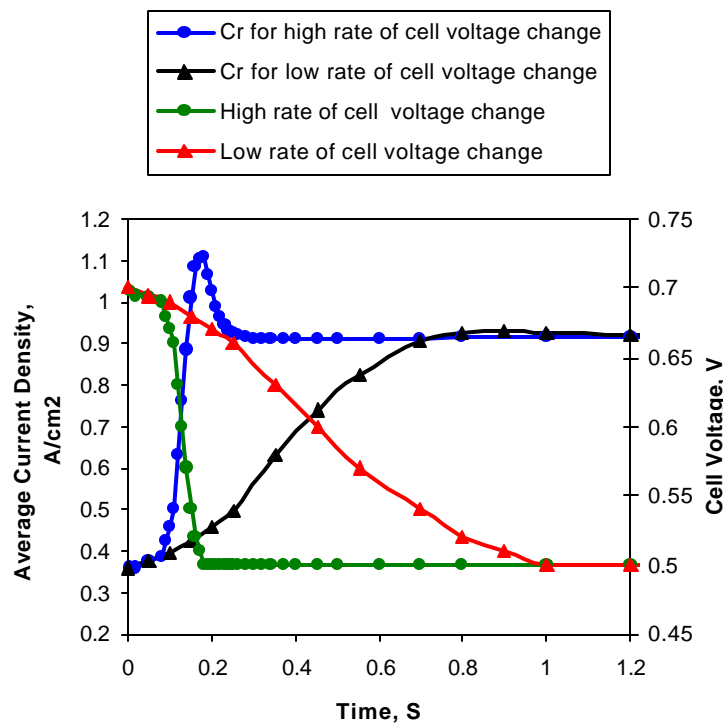


Fig. 7. Transient response of average current density with different cell voltage incremental change from 0.7V to 0.5V.

Figure 7 illustrates the transient current response with two different incremental voltage changes as revealed in Fig. 5. This figure confirms that the magnitude of current density

overshoot is affected by the rate of change of cell voltage. For the rate of change of cell voltage corresponding to condition # 3 in Fig. 5, the maximum average current density reaches  $0.92 \text{ A/cm}^2$  at  $t=0.8 \text{ s}$  and cell voltage of  $0.52 \text{ V}$ . The current density reaches steady state value of  $0.91 \text{ A/cm}^2$  at  $t=1.0 \text{ s}$ . If the rate of cell voltage change is carried out with proper slope, the current density overshoot can be completely eliminated as in Fig. 7. This was accomplished by reducing the cell voltage from  $0.7 \text{ V}$  to  $0.5 \text{ V}$  in  $18 \text{ s}$  time with small incremental changes both in time and cell voltage. The result is shown in Figure 8 (the figure at the end of this document can be added or not). The study shows that the same can be accomplished in shorter time of about  $1 \text{ s}$  if proper slope for the cell voltage change is implemented. It was established that the slope of cell voltage change should be small when it is reaching the steady state condition of  $0.5 \text{ V}$  if the overshoot needs to be eliminated.

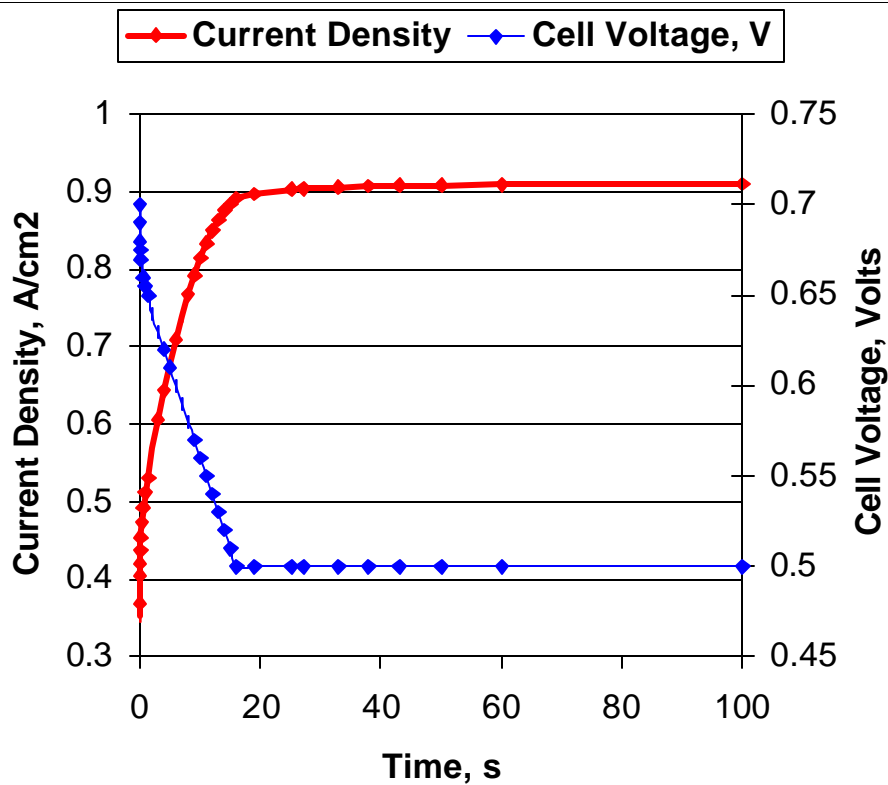
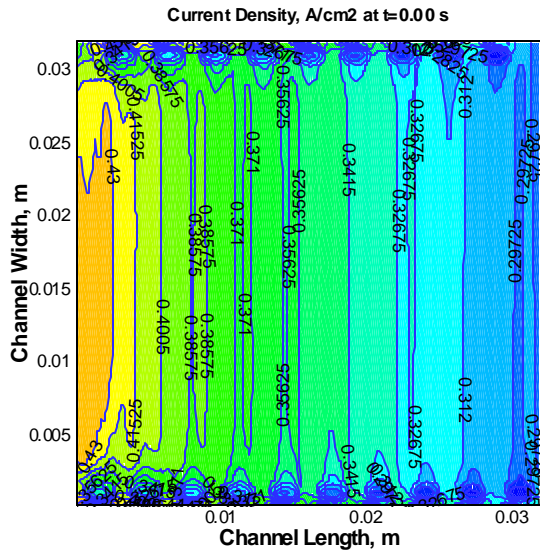
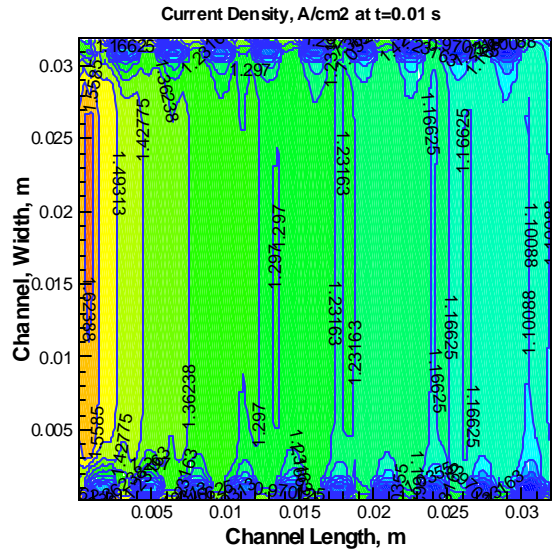


Fig. 8. Incremental cell voltage change with no overshoot for Current Density.

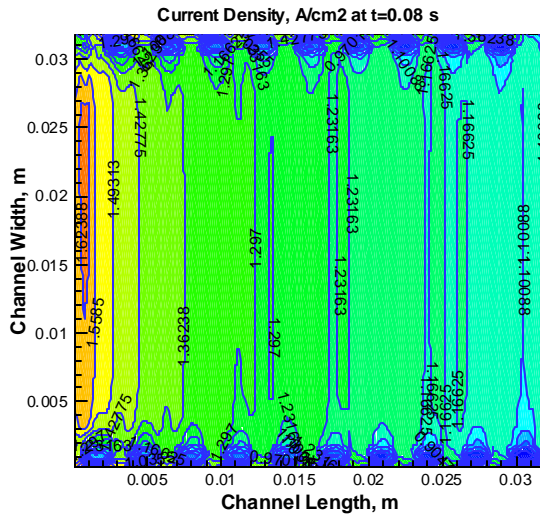
Fig. 9 shows the local current density on the membrane surface at four different time steps and cell voltages for condition #1, step change. These figures show that there are spatial variations of local current density values, which cannot be provided, in one-dimensional and two-dimensional models. At the steady state corresponding to the cell voltage of 0.7 V and  $t=0.0$  s, the local current density is higher in the inlet region and decreases along the flow channel towards the outlet due to the reduction of anode activity of water. The maximum and minimum local densities are  $0.431 \text{ A/cm}^2$  and  $0.303 \text{ A/cm}^2$  respectively, which represents small variation over the entire active cell area. There are also current density variations along the channel bends, where the higher current density is situated outside of the bends. This is because the sharp edges along the bends produce re-circulation zones around the outward corners (edges), resulting in higher velocities and hence higher gas concentrations at the inner corners than the outer corners. When the cell voltage is changed to drop to 0.5 V in 0.01 s time, the local current density significantly increases over the membrane surface but the contour pattern is similar to the previous figure. The highest local current density is  $1.624 \text{ A/cm}^2$  and the lowest value is  $0.970 \text{ A/cm}^2$ . When the time increases to 0.08 s, there is more non-uniformity of local current density distribution. The local current density reduces considerably in the region from the center of membrane surface toward the outlet due to decreasing of oxygen concentration. The highest local current density is located around the inlet with a value of  $1.739 \text{ A/cm}^2$  and the lowest local current density is at the outlet with a value of  $0.634 \text{ A/cm}^2$ . When the time reaches 10 s, the local current density decreases from the center region of the membrane surface towards the outlet region. The current density in this case varies from  $1.714 \text{ A/cm}^2$  to  $0.270 \text{ A/cm}^2$ , which represents considerable variations along the membrane surface. It is noted that after the cell voltage is for the case under consideration, at steady state cell voltage of 0.5 V, the local current



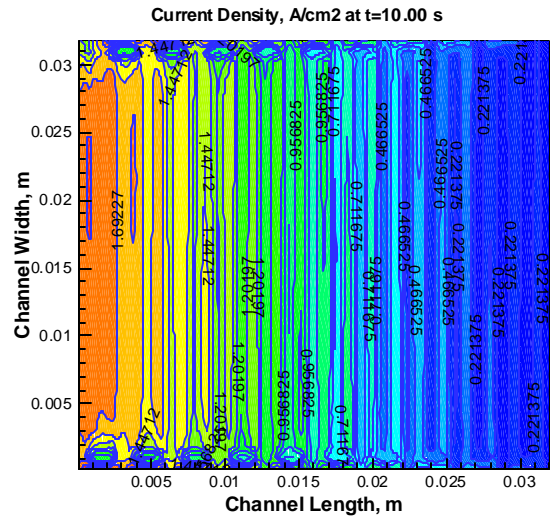
$V_{cell} = 0.7$  Volts



$V_{cell} = 0.5$  volts



$V_{cell} = 0.5$  volts



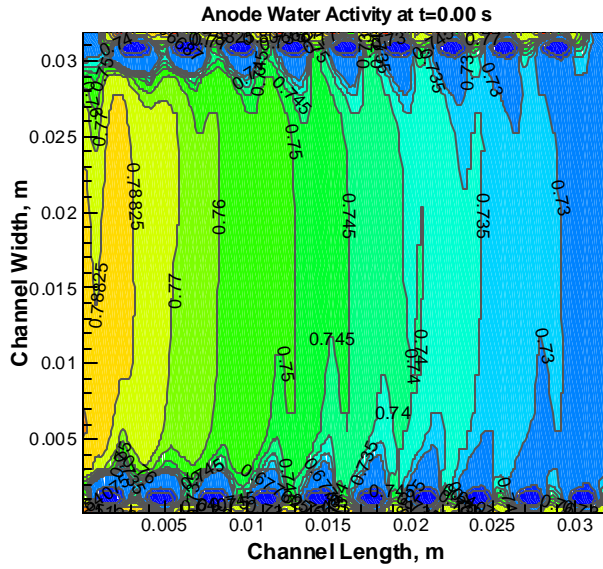
$V_{cell} = 0.5$  volts

Fig. 9. Local transient current density (A/cm<sup>2</sup>) contours at different time steps and cell voltages for step cell voltage change condition (Condition #1)

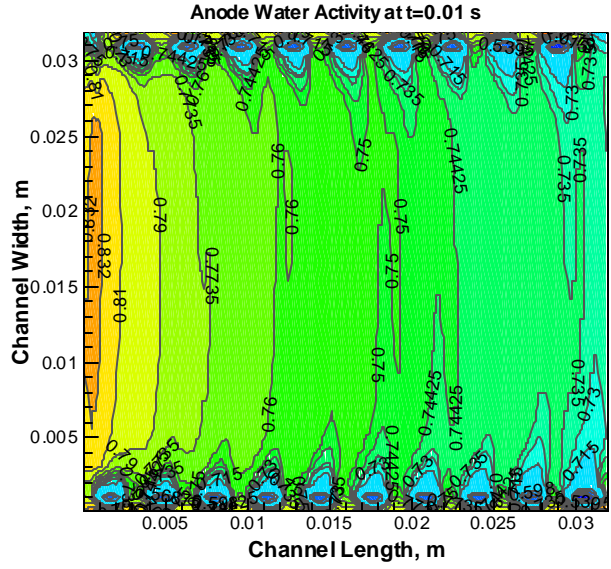
density does not significantly vary over the first half of the membrane surface, but it sharply decreases over the second half of membrane surface. This is because the high reaction rate regions accompany excessive hydrogen and oxygen consumptions and therefore they are depleted in these regions.

Fig. 10 shows the transient local oxygen mole fraction contours on the membrane surface for different time steps and cell voltages. The figures reveal that the local oxygen mole fraction patterns are analogous to the local current density contours. When the cell voltage is changed to 0.5 V with a time step of 0.01 s, the oxygen mole fraction becomes quite non-uniform staging a rapid depletion towards the outlet regions of the membrane surface. The decrease of oxygen mole fraction in the inlet region of the membrane cell is about 18%, whereas the decrease is about 30% for the outlet region. Comparison of the four time step contours shows that the oxygen mole fraction in the inlet area of the membrane surface reaches its steady state value of 0.09 (a 38% reduction) in a time span of 0.1 s. Whereas, it reaches the steady value of 0.002 (a 98% reduction) over the outlet 50% area of the membrane in 10 s time. Under these conditions, there is not enough oxygen for reactions in the outlet 50% area of the cell membrane, which can cause the resulting decrease of current density in this region.

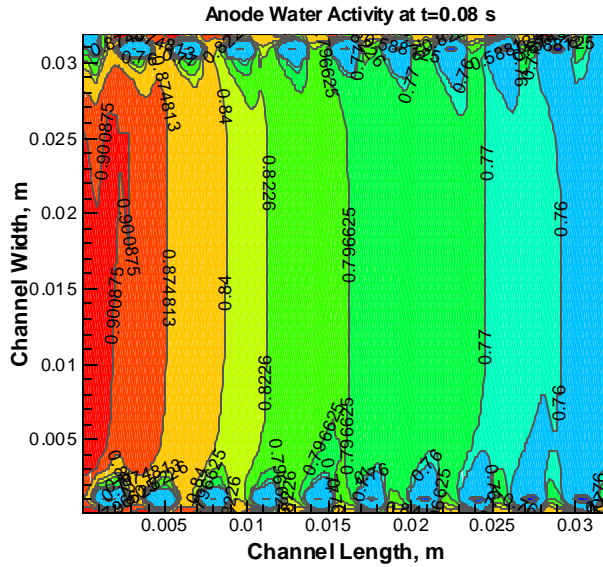




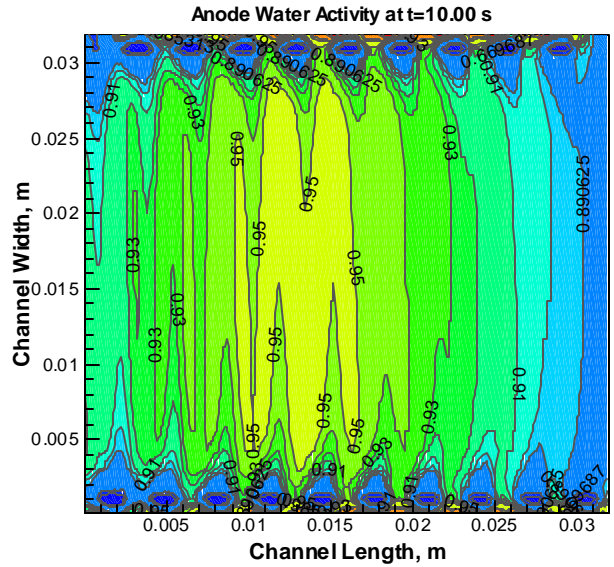
$V_{cell} = 0.7$  Volts



$V_{cell} = 0.5$  Volts



$V_{cell} = 0.5$  Volts

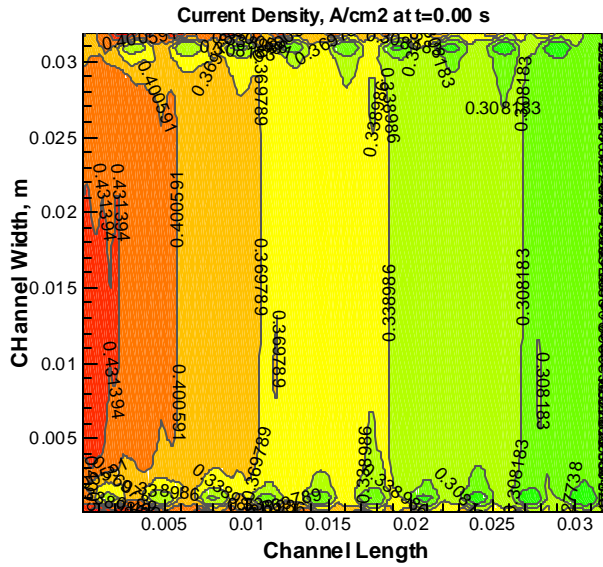


$V_{cell} = 0.5$  Volts

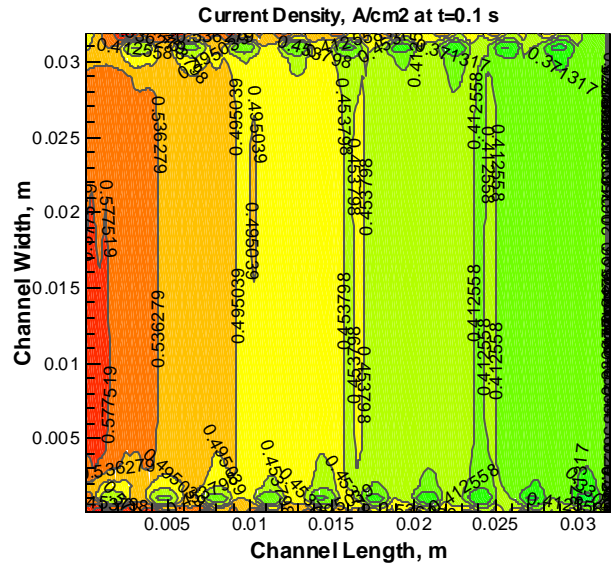
Fig. 11. Local Transient anode water activity contours at different times and cell voltages for step cell voltage change condition (Condition #1).

Fig. 11 shows the transient local anode water activity contours on the membrane surface for condition #1. Comparison of the four figures for the four time steps expose the small variation of local anode activity on the entire membrane surface which is due to the rate of water transport or net water transfer coefficient per proton, which is a function of electro-osmotic drag of anode water content and concentration gradient between the cathode and anode water. The figures at the indicated time steps of 0.0 s, 0.01 s, and 0.08 s with cell voltages of 0.7 V, 0.50 V, and 0.50 V respectively, indicate that the anode activity is highest in the inlet region and lowest at near the outlet. This is in good agreement with contour patterns of local current density in Fig. 9. When time reaches 10.0 s, the water activity increases from inlet to just about the center of the membrane surface due to water back diffusion from cathode to anode. Subsequently, the water activity starts to decrease toward the outlet area as a result of anode water transport to cathode by electro-osmotic drag.

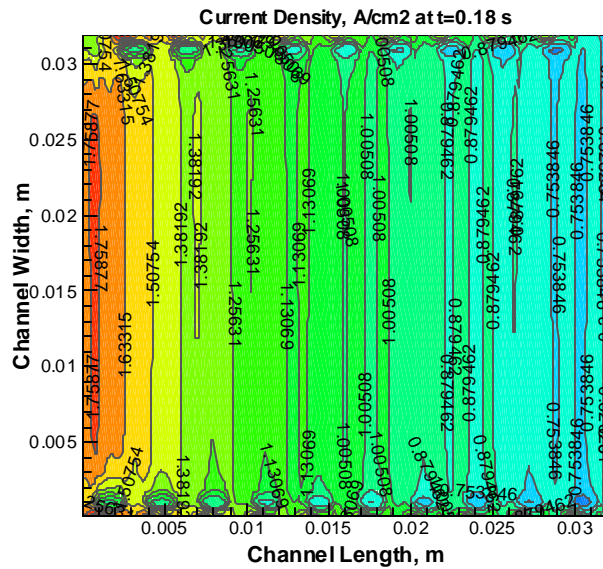
There is a marked difference in transient local current density contours when the results of case 2 and case 3 for the incremental change of cell voltage (Figs. 12 and 13) are compared with the results of case 1 which the cell voltage is changed in one step (Fig. 9). At time  $t=0.0$  s the current density contour plot is the same for all three cases. In general, the current density contours for each time step gradually decrease from the inlet to the outlet. The major difference for the three cases is when they are compared for the time step at which the maximum overshoot occurs. The magnitude of the current density for all three cases is comparable in the immediate inlet region of the cell. But, for the incremental cell voltage changes, the current density has higher rate of decrease towards the outlet region. At this peak condition, the current density distribution is more uniform for cases with more rapid cell voltage change. The current density drop is heightened for case #3 with slower rate of cell voltage change. As a result, the amount of



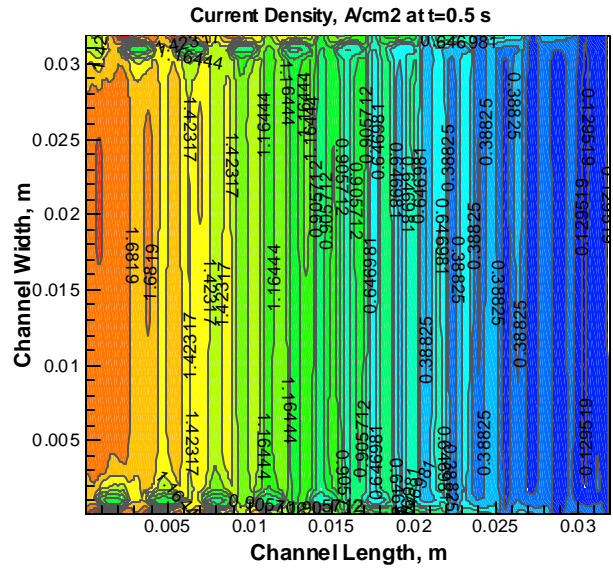
$V_{cell} = 0.7$  Volts



$V_{cell} = 0.67$  volts



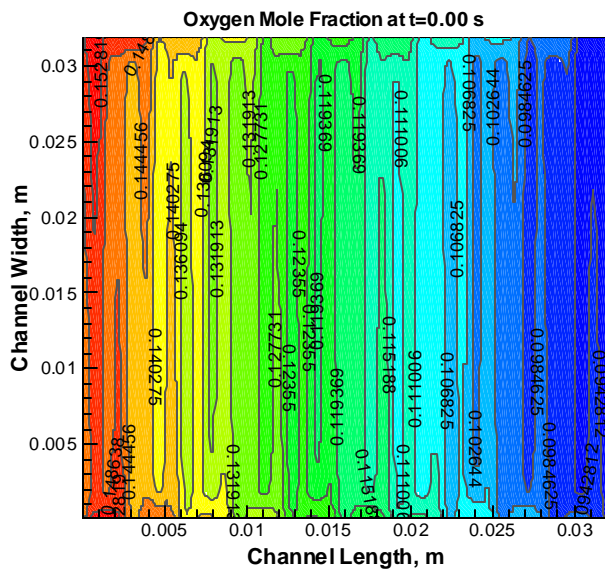
$V_{cell} = 0.5$  Volts



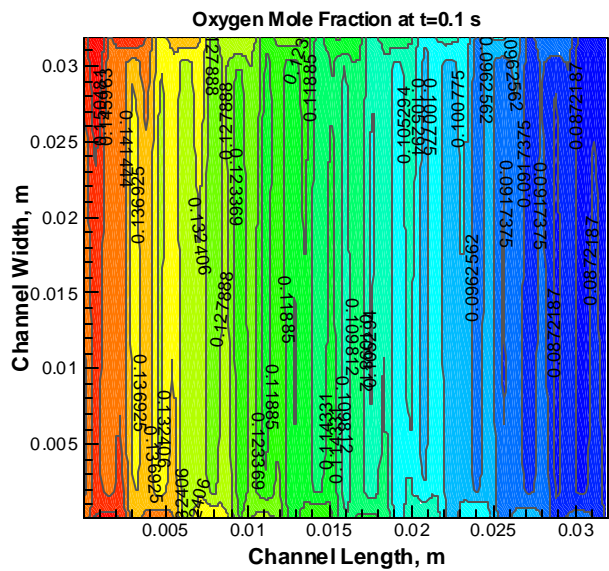
$V_{cell} = 0.5$  volts

Fig. 12. Local transient Current Density ( $A/cm^2$ ) contours at different times and cell voltages for incremental cell voltage change condition (Condition #2).

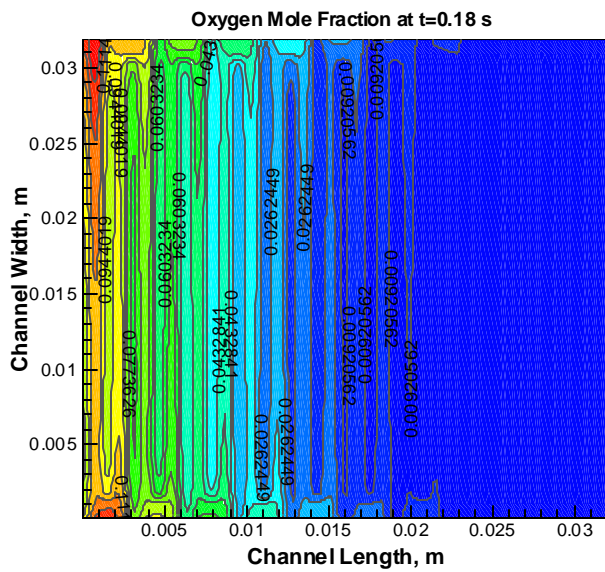




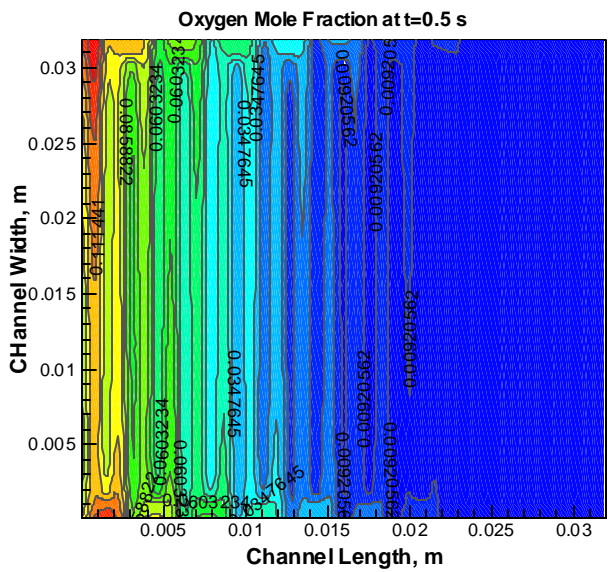
$V_{cell} = 0.7$  Volts



$V_{cell} = 0.67$  volts



$V_{cell} = 0.5$  Volts

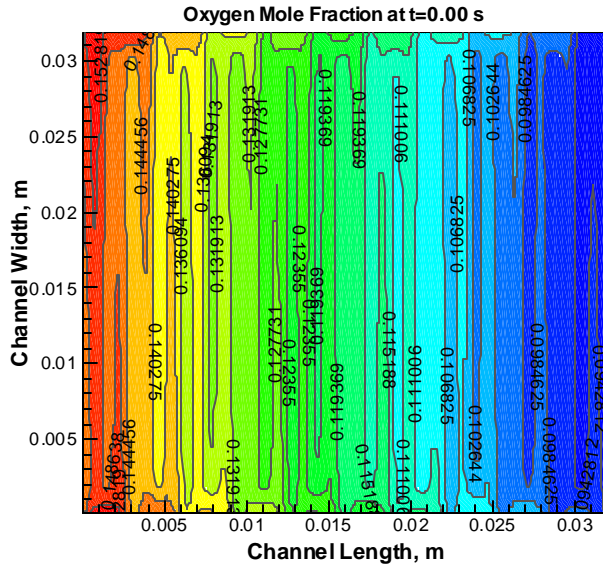


$V_{cell} = 0.5$  volts

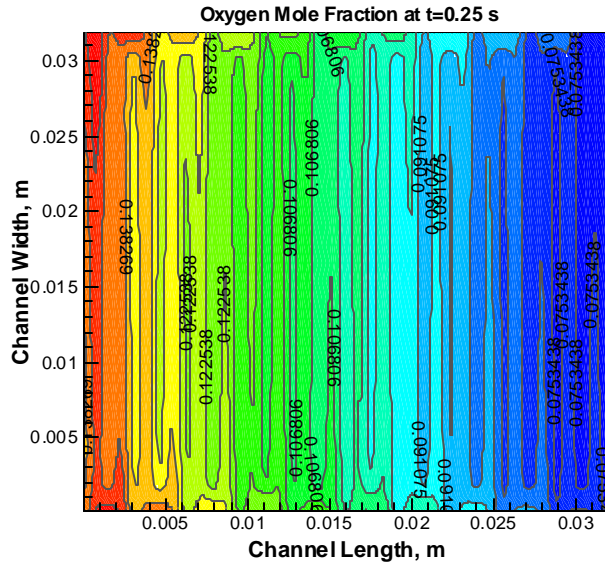
Fig. 14. Local transient Oxygen Mole Fraction contours at different time and cell voltage for incremental cell voltage change condition (Condition #2)

overshoot for the average current density is lower for case #3. Moreover, the local numerical values of the current density depend on the concentration of the reacting gases, particularly oxygen under these operating conditions. The final contours of both Figs. 12 and 13 represent the local current density contours at the steady state. These contours for both figures are alike and similar to the case of step cell voltage change (condition #1).

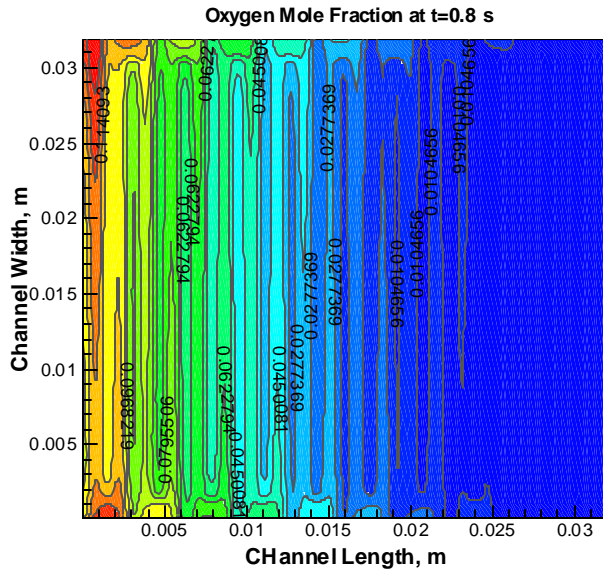
Figs. 14 and 15 show the transient local oxygen mole fraction for incremental voltage change of conditions 2 and 3 respectively. The time steps and cell voltages shown in Figs. 14 and 15 correspond to Figs. 12 and 13 respectively. These figures verify that the variation of local current density for the specified stoics, cell voltage and time step change is due to the local oxygen concentration. The oxygen decreases from the center of membrane surface and is almost depleted toward the outlet when cell voltage is decreased to its steady state value.



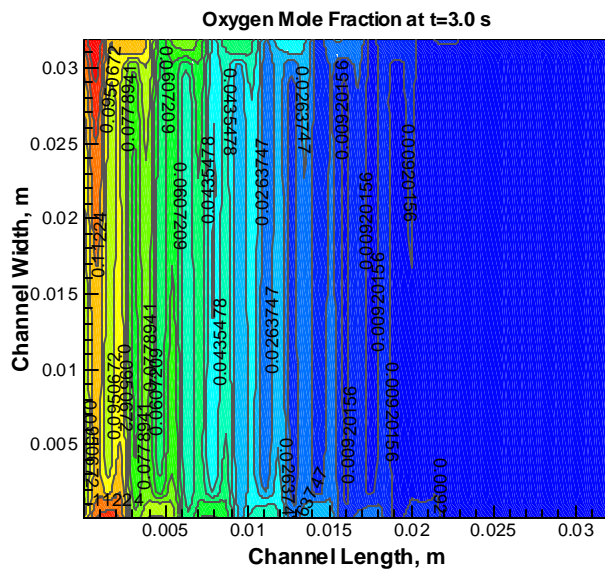
$V_{cell} = 0.7$  Volts



$V_{cell} = 0.66$  volts



$V_{cell} = 0.61$  Volts



$V_{cell} = 0.5$  volts

Fig. 15. Local transient Oxygen Mole Fraction contours at different times and cell voltages for incremental cell voltage change condition (Condition #3)

**Table 1: Governing equations and source terms.**

Governing Equations	Mathematical expressions	Non-zero volumetric source terms and location of application (see Fig. 2)
Conservation of mass	$\frac{\partial \mathbf{r}}{\partial t} + \frac{\partial(\mathbf{ru})}{\partial x} + \frac{\partial(\mathbf{rv})}{\partial y} + \frac{\partial(\mathbf{rw})}{\partial z} = S_m \quad (1)$	$S_m = S_{H_2} + S_{aw} \text{ at } z = z_3$ $S_m = S_{O_2} + S_{cw} \text{ at } z = z_2$ <p>(7)</p>
Momentum transport	$\frac{\partial(\mathbf{ru})}{\partial t} + u \frac{\partial(\mathbf{ru})}{\partial x} + v \frac{\partial(\mathbf{ru})}{\partial y} + w \frac{\partial(\mathbf{ru})}{\partial z} = -\frac{\partial P}{\partial x} + \frac{\partial}{\partial x} \left( \mathbf{m} \frac{\partial u}{\partial x} \right) + \frac{\partial}{\partial y} \left( \mathbf{m} \frac{\partial u}{\partial y} \right) + \frac{\partial}{\partial z} \left( \mathbf{m} \frac{\partial u}{\partial z} \right) + S_{px}$ $\frac{\partial(\mathbf{rv})}{\partial t} + u \frac{\partial(\mathbf{rv})}{\partial x} + v \frac{\partial(\mathbf{rv})}{\partial y} + w \frac{\partial(\mathbf{rv})}{\partial z} = -\frac{\partial P}{\partial y} + \frac{\partial}{\partial x} \left( \mathbf{m} \frac{\partial v}{\partial x} \right) + \frac{\partial}{\partial y} \left( \mathbf{m} \frac{\partial v}{\partial y} \right) + \frac{\partial}{\partial z} \left( \mathbf{m} \frac{\partial v}{\partial z} \right) + S_{py}$ $\frac{\partial(\mathbf{rw})}{\partial t} + u \frac{\partial(\mathbf{rw})}{\partial x} + v \frac{\partial(\mathbf{rw})}{\partial y} + w \frac{\partial(\mathbf{rw})}{\partial z} = -\frac{\partial P}{\partial z} + \frac{\partial}{\partial x} \left( \mathbf{m} \frac{\partial w}{\partial x} \right) + \frac{\partial}{\partial y} \left( \mathbf{m} \frac{\partial w}{\partial y} \right) + \frac{\partial}{\partial z} \left( \mathbf{m} \frac{\partial w}{\partial z} \right) + S_{pz}$ <p>(2)</p>	$S_{px} = -\frac{\mathbf{m}u}{\mathbf{b}_x};$ $S_{py} = -\frac{\mathbf{m}v}{\mathbf{b}_y};$ $S_{pz} = -\frac{\mathbf{m}w}{\mathbf{b}_z}$ <p>at <math>z_1 \leq z \leq z_4</math></p> <p>(8)</p>
Hydrogen transport (anode side)	$\frac{\partial(\mathbf{rm}_{H_2})}{\partial t} + u \frac{\partial(\mathbf{rm}_{H_2})}{\partial x} + v \frac{\partial(\mathbf{rm}_{H_2})}{\partial y} + w \frac{\partial(\mathbf{rm}_{H_2})}{\partial z} = \frac{\partial(J_{x,H_2})}{\partial x} + \frac{\partial(J_{y,H_2})}{\partial y} + \frac{\partial(J_{z,H_2})}{\partial z} + S_{H_2} \quad (3)$	$S_{H_2} = -\frac{I(x,y)}{2F} M_{H_2} A_{cv} \text{ at } z = z_3$ <p>(9)</p>
Water transport (anode side)	$\frac{\partial(\mathbf{rm}_{aw})}{\partial t} + u \frac{\partial(\mathbf{rm}_{aw})}{\partial x} + v \frac{\partial(\mathbf{rm}_{aw})}{\partial y} + w \frac{\partial(\mathbf{rm}_{aw})}{\partial z} = \frac{\partial(J_{x,aw})}{\partial x} + \frac{\partial(J_{y,aw})}{\partial y} + \frac{\partial(J_{z,aw})}{\partial z} + S_{aw} \quad (4)$	$S_{aw} = -\frac{\mathbf{a}(x,y)}{F} I(x,y) M_{H_2O} A_{cv}$ <p>at <math>z = z_3</math></p> <p>(10)</p>
Oxygen transport (cathode side)	$\frac{\partial(\mathbf{rm}_{O_2})}{\partial t} + u \frac{\partial(\mathbf{rm}_{O_2})}{\partial x} + v \frac{\partial(\mathbf{rm}_{O_2})}{\partial y} + w \frac{\partial(\mathbf{rm}_{O_2})}{\partial z} = \frac{\partial(J_{x,O_2})}{\partial x} + \frac{\partial(J_{y,O_2})}{\partial y} + \frac{\partial(J_{z,O_2})}{\partial z} + S_{O_2} \quad (5)$	$S_{O_2} = -\frac{I(x,y)}{4F} M_{O_2} A_{cv}$ <p>at <math>z = z_2</math></p> <p>(11)</p>
Water transport (cathode side)	$\frac{\partial(\mathbf{rm}_{cw})}{\partial t} + u \frac{\partial(\mathbf{rm}_{cw})}{\partial x} + v \frac{\partial(\mathbf{rm}_{cw})}{\partial y} + w \frac{\partial(\mathbf{rm}_{cw})}{\partial z} = \frac{\partial(J_{x,cw})}{\partial x} + \frac{\partial(J_{y,cw})}{\partial y} + \frac{\partial(J_{z,cw})}{\partial z} + S_{cw} \quad (6)$	$S_{cw} = \frac{I+2\mathbf{a}(x,y)}{2F} I(x,y) M_{H_2O} A_{cv}$ <p>at <math>z = z_2</math></p> <p>(12)</p>

**Table 2. Equations for modeling electrochemical effects.**

Diffusion mass flux of species $l$ in $\xi$ direction	$J_{i,l} = -\mathbf{r}D_{i,l}\frac{\partial m_{K,l}}{\partial \mathbf{x}}$
	(13)
Binary diffusion coefficient [11]	$\frac{PD_{i,j}(x,y)}{(P_{c-i} * P_{c-j})^{1/3} \cdot (T_{c-i} \cdot T_{c-j})^{5/12} \cdot (\frac{1}{M_i} + \frac{1}{M_j})^{1/2}} = 3.64 \times 10^{-8} \left( \frac{T_{cell}}{\sqrt{T_{c-i} \cdot T_{c-j}}} \right)^{2.334}$ (14)
Net water transfer coefficient per proton	$\mathbf{a}(x,y) = n_d(x,y) - \frac{F}{I(x,y)} D_W(x,y) \frac{(C_{wc}(x,y) - C_{wa}(x,y))}{t_m}$
	(15)
Water content in the membrane	$\mathbf{I} = 0.043 + 17.81a_a - 39.85a_a^2 + 36.0a_a^3; 0 < a_a \leq 1$ $= 14 + 1.4(a_a - 1); 1 < a_a \leq 3$
	(16)
Electro-osmotic drag coefficient	$n_d = 0.0029\mathbf{I}^2 + 0.05\mathbf{I} - 3.4 \times 10^{-19}$
	(17)
Water diffusion coefficient	$D_w = n_d 5.5 \times 10^{-11} \exp \left[ 2416 \left( \frac{1}{303} - \frac{1}{T_s} \right) \right]$
	(18)
Water concentration for anode and cathode surfaces of the MEA	$C_{wK}(x,y) = \frac{\mathbf{r}_{m,dry}}{M_{m,dry}} (0.043 + 17.8a_K - 39.8a_K^2 + 36.0a_K^3); a_K \leq 1$ $= \frac{\mathbf{r}_{m,dry}}{M_{m,dry}} (14 + 1.4(a_K - 1)); \text{for } a_K > 1, \text{ where } K = a \text{ or } c$
	(19)
Water activity	$a_K = \frac{X_{w,K} P(x,y)}{P_{w,K}^{sat}}$
	(20)
Local current density	$I(x,y) = \frac{\mathbf{s}_m(x,y)}{t_m} \{V_{oc} - V_{cell} - \mathbf{H}(x,y)\}$
	(21)
Local membrane conductivity	$\mathbf{s}_m(x,y) = \left( 0.00514 \frac{M_{m,dry}}{\mathbf{r}_{m,dry}} C_{wa}(x,y) - 0.00326 \right) \exp \left( 1268 \left( \frac{1}{303} - \frac{1}{T_s} \right) \right) \times 10^2$ (22)
Local over-potential	$\mathbf{H}(x,y) = \frac{RT_s}{0.5F} \ln \left[ \frac{I(x,y)P(x,y)}{I_{oO_2} P_{O_2}(x,y)} \right] + \frac{RT_s}{0.5F} \ln \left[ \frac{I(x,y)P(x,y)}{I_{oH_2} P_{H_2}} \right]$
	(23)
Viscosity of mixture	$\mathbf{m} = \sum_i m_i \mathbf{m}_i$
	(24)

**Table 3. Inlet conditions and parameters**

Cell voltage	Volts	0.5	0.7
Anode channel inlet conditions	Velocity ( $\text{m s}^{-1}$ )	2.6	1.2
	Mole fraction of $\text{H}_2$	0.729	0.759
	Mole fraction of $\text{H}_2\text{O}$	0.271	0.241
Cathode channel inlet conditions	Velocity ( $\text{m s}^{-1}$ )	9.9	4.5
	Mole fraction of $\text{O}_2$	0.165	0.170
	Mole fraction of $\text{N}_2$	0.622	0.638
	Mole fraction of $\text{H}_2\text{O}$	0.213	0.192
Operating conditions	Operating Pressure (atm)	1	1
	Cell Voltage (V)	0.5	0.7
	Permeability of diffusion layer ( $\times 10^{+15} \text{ m}^2$ )	3.3	3.3
Membrane thickness ( $\mu\text{m}$ )	50		

**Table 4. VI data**

Cell Voltage	0.9	0.8	0.7	0.6	0.5	0.4	0.3
CR-Experiment	0	0.08	0.4	0.67	0.85	1	1.09
CR-Numerical	0	0.12	0.34	0.76	1.03	1.2	1.28

## **Conclusions**

A three-dimensional time dependent simulation of PEM fuel cell was developed with a variable load. Different rates of load change were selected to study their effects on the PEM fuel cell performance. Contours of local current density, anode water activity, and oxygen concentration were presented and discussed.

For the particular operating conditions and properties used in this study, the results indicate that there can be current overshoot when the cell voltage is reduced. This overshoot can create the instability of fuel cell performance. However, the peak of current overshoot can be reduced or eliminated by controlling the rate at which the cell voltage is changed. Smaller slopes for the cell voltage change with time curve; decreases the peak of current overshoot but creates added non-uniformity in the current density contour. Nevertheless, the non-uniformity of local current density distribution is also dependent on anode water activity and local concentration of the reacting gases, especially the oxygen concentration for the conditions of this study. These results can help our on-going works in order to redesign flow-field plate configuration, operating of gases flow rates, and rate of load changes. These design changes should improve the undesirable fuel cell performance such as the current overshoot as a result of load change, and will increase the performance dramatically.

## **Acknowledgements**

The authors wish to acknowledge the financial support of this work by South Carolina State University/University Transportation Center (Grant no. 2000-013), and Department of Energy-EPSCoR (Grant no. DE-FG02-91ER75666).

## LIST OF SYMBOLS

$a_K$	=	activity of water in stream K, dimensionless
$A_{cv}$	=	specific surface area of the control volume (c.v.), $m^{-1}$
$C$	=	condensation rate ( $s^{-1}$ )
$C_{wK}$	=	concentration of water vapor at K interface of the membrane, $mol\ m^{-3}$
$D_h$	=	hydraulic diameter of flow channel, m
$D_{n,j}$	=	binary diffusion coefficient of species n in mixture j, $m^2\ s^{-1}$
$D_w$	=	diffusion coefficient of water, $m^2\ s^{-1}$
$F$	=	Faraday constant, 96487 C mole-of-electrons $^{-1}$
$I$	=	local current density, $A\ m^{-2}$
$I_o$	=	exchange current density $A\ m^{-2}$
$m_{n,K}$	=	mass fraction of the species n in stream K, dimensionless
$M_{m,dry}$	=	equivalent weight of a dry membrane, $kg\ mol^{-1}$
$M_n$	=	molecular weight of species n, $kg\ mol^{-1}$
$mass_n$	=	mass of species n, kg
$n_d$	=	electro-osmotic drag coefficient (number of water molecules carried per proton)
$P_{w,K}^{sat}$	=	vapor pressure of water in stream K, Pa
$P$	=	pressure, Pa
$P_n$	=	partial pressure of species n, Pa
$Q$	=	volume flow rate, $m^3/s$
$R$	=	universal gas constant, $8.314\ J\ mol^{-1}\ K^{-1}$
$S$	=	source term
$t$	=	time (s)
$t_m$	=	membrane thickness, m
$T$	=	temperature, K
$u, v, w$	=	velocities in x, y, and z directions respectively, $m\ s^{-1}$
$V_{oc}$	=	cell open-circuit voltage, V
$V_{cell}$	=	cell voltage, V
$x$	=	channel length measured from anode inlet, m
$X_{w,K}$	=	mole fraction of water in stream K

### Greek symbols

<b><math>a</math></b>	=	net water flux per proton flux
$\beta_\xi$	=	permeability in the $\xi$ direction
<b><math>h</math></b>	=	overpotential for oxygen reaction, V
<b><math>l</math></b>	=	water content in the membrane
<b><math>m</math></b>	=	dynamic viscosity, $kg\ s\ m^{-2}$
$r_{m,dry}$	=	density of a dry membrane, $kg\ m^{-3}$
<b><math>r</math></b>	=	density of the mixture, $kg\ m^{-3}$
<b><math>S_m</math></b>	=	membrane conductivity, $ohm^{-1}\ m^{-1}$

### Subscripts and superscripts

$a$	=	anode
$c$	=	cathode

$CO_2$	=	carbon dioxide
$e$	=	electrochemical reaction
$H_2$	=	hydrogen
$K$	=	anode or cathode
$N_2$	=	nitrogen
$O_2$	=	oxygen
$p$	=	phase change
$v$	=	vapor
$w$	=	water
$sat$	=	saturated
$\xi$	=	dummy variable for direction x, y, or z.

## REFERENCES

1. T. E. Springer, T. A. Zawodzinski, and S. Gottesfeld, *J. of Electrochem. Soc.*, **138**, 2334 (1991).
2. D. M. Bernardi and M. W. Verbrugge, *AIChE J.*, **37**, 1151 (1991).
3. D. M. Bernardi and M. W. Verbrugge, 1992, *J. Electrochem. Soc.*, **139**, 2477 (1992).
4. T. Fuller and J. Newman, *J. of Electrochem. Soc.*, **140**, 1218 (1993).
5. T. Nguyen and R. White, *J. of Electrochem. Soc.*, **140**, 2178 (1993).
6. A. West and T. Fuller, *J. of Applied Electrochemistry*, **26**, 557 (1996).
7. J. Yi and T. Nguyen, *J. of Electrochem. Soc.*, **145**, 1149 (1998).
8. J. Yi and Y. Nguyen, *J. of Electrochem. Soc.*, **146**, 38 (1999).
9. V. Garua, H. Liu, S. Kakac, *J. of AIChE*, **44**, 2410 (1998).
10. A. Kazim, H. Liu, and P. Forges, *J. of Applied Electrochemistry*, **29**, 1409 (1999).
11. A. Kulikovskiy, J. Divisek, and A. Kornyshev, *J. of Electrochem. Soc.*, **146**, 3981 (1999).
12. S. Shimpalee, *Ph.D. dissertation*, Dept. of Mechanical Engineering, University of South Carolina, SC. (2001).
13. H. Naseri-Neshat, S. Shimpalee, S. Dutta, W.K. Lee, and J. W. Van Zee, in *Proceeding of ASME IMECE*, Nashville, TN., **4**, 341 (1999).
14. S. Shimpalee, S. Dutta, W.K. Lee, and J. W. Van Zee, in *Proceeding of ASME IMECE*, Nashville, TN., **5**, 464 (1999).
15. S. Shimpalee, W.K. Lee, S. Dutta, and J. W. Van Zee, submitted to *J. Electrochem. Soc.*, (2001).
16. S. Dutta, S. Shimpalee, and J. W. Van Zee, *Intl. J. of Heat and Mass Transfer*, **44/11**, 2029 (2001).
17. W.K. Lee, J. W. Van Zee, S. Shimpalee, and S. Dutta 1999, in *Proceeding of ASME IMECE*, Nashville, TN., **5**, 454 (1999).
18. S. Shimpalee and S. Dutta, *Numerical Heat Transfer*, Part A, **38**, 111 (2000).
19. S. Um and C. Y. Wang, in *Proceeding of ASME IMECE*, Orlando, FL., **1**, 19 (2000).
20. T. Zhou and H. Liu, in *Proceeding of ASME IMECE*, Orlando, FL., **1**, 43 (2000).
21. S. Shimpalee, S. Dutta, and J. W. Van Zee, *Proceeding. of ASME IMECE*, Orlando, FL., **1**, 1 (2000).
22. S. Um, C. Y. Wang, and K. S. Chen, 2000, *J. of Electrochem. Soc.*, **147**, 4485 (2000).
23. S. Shimpalee, W-K. Lee, J. W. Van Zee, and H. Naseri-Neshat, in *Proceeding of the 01 IECEC*, Savannah, GA (2001).

24. R. B. Bird, W. E. Stewart, and E. N. Lightfoot, *Transport Phenomena*, John Wiley & Sons, New York (1960).
25. S. V. Patankar, *Numerical Heat Transfer and Fluid Flow*, Hemisphere, New York (1980)

